Sol gel graphene/TiO$_2$ nanoparticles for the photocatalytic-assisted sensing and abatement of NO$_2$

Andrea Giampiccolo[a,*], David Maria Tobaldi[b], Salvatore Gianluca Leonardi[c],
Billy James Murdoch[d,1], Maria Paula Seabra[b], Martin P. Ansell[a], Giovanni Neri[c], Richard J. Ball[a,*]

[a] BRE Centre for Innovative Construction Materials, Department of Architecture and Civil Engineering, University of Bath, Bath, BA2 7AY, UK
[b] Department of Materials and Ceramic Engineering, CICECO – Aveiro Institute of Materials, University of Aveiro, Campus Universitário de Santiago, 3810-193 Aveiro, Portugal
[c] Department of Engineering, University of Messina, C.da Di Dio, I-98166 Messina, Italy
[d] National EPSRC XPS Users' Service (NEXUS), School of Mechanical and Systems Engineering, Newcastle University, Newcastle upon Tyne, Tyne and Wear, NE1 7RU, UK

ARTICLE INFO

ABSTRACT

Human exposure to volatile organic compounds and NO$_2$ can lead to health problems, therefore strategies to mitigate against the risks are required. Abatement and sensing are approaches which could both neutralise and monitor these species thus providing a safer environment and warning occupants of harmful levels. This paper presents pure TiO$_2$ and TiO$_2$/graphene hybrids synthesized through a sol-gel route. Electron optical, helium ion microscopy, X-ray diffraction and spectroscopic methods have been applied to elucidate the physical and chemical behaviour. NO$_2$ sensing properties of TiO$_2$/graphene hybrids formed by the addition of graphene to the reaction vessel prior to initiating the sol gel reaction followed by annealing (**GTiO$_2$S),** and an alternative manufacturing method involving the addition of graphene to TiO$_2$ nanoparticles which had already been annealed (**GTiO$_2$M**) were compared and evaluated. A conductometric sensor based on TiO$_2$/graphene prepared using material **GTiO$_2$S** showed a higher response to NO$_2$ compared to sensors based on pure TiO$_2$ and TiO$_2$/graphene prepared with material **GTiO$_2$M**. Under UV irradiation generated by a low power LED, the sensor showed a remarkably enhanced response to 1750 ppb NO$_2$, about double the response in the dark, and a limit of detection of about 50 ppb of NO$_2$ (Signal/Noise = 3). Photocatalytic tests to assess the degradation of NO$_x$ showed that TiO$_2$/graphene hybrids using material **GTiO$_2$S** were the most active amongst the whole series of TiO$_2$-based materials. Our data highlights the unique characteristics of material **GTiO$_2$S** TiO$_2$/graphene and the suitability for multi-purpose applications in the field of environmental monitoring and remediation. The capability of the material for both sensing and abatement of NO$_x$ could be exploited to offer a safer environment through providing a warning of the presence of NO$_x$ whilst also reducing levels.

1. Introduction

Awareness of the health risks associated with the presence of atmospheric pollutants and volatile organic compounds (VOCs) in the indoor and outdoor environment is stimulating research aimed at improving air quality. In the UK each year approximately 40,000 deaths can be attributed to outdoor air pollution. Many major health challenges of modern societies such as cancer, asthma, stroke, heart disease, diabetes, obesity and dementia can be linked to air pollution. The

development of materials with the ability to detect and neutralise air pollutants are important for emerging technologies which will mitigate their harmful effects. Since the discovery of the photocatalytic (PC) water splitting properties of TiO$_2$ by Honda and Fujishima in 1972 [1], the application of semiconductors, such as titanium dioxide (TiO$_2$), for the photo-degradation of VOCs and inorganic pollutants has increased exponentially in the last 30 years [2–5]. The extensive use of TiO$_2$ is attributed to the ratio of cost to PC activity, low toxicity and its band gap of 3.2 eV (when in the anatase polymorph) that is activated when

---

* Corresponding authors.
E-mail addresses: A.Giampiccolo@bath.ac.uk (A. Giampiccolo), david.tobaldi@ua.pt, david@davidtobaldi.org (D.M. Tobaldi),
leonardis@unime.it (S.G. Leonardi), billy.murdoch@rmit.edu.au (B.J. Murdoch), pseabra@ua.pt (M.P. Seabra), M.P.Ansell@bath.ac.uk (M.P. Ansell),
gneri@unime.it (G. Neri), R.J.Ball@bath.ac.uk (R.J. Ball).
[1] Currently at School of Science, RMIT University, VIC 3001, Melbourne, Australia.

the semiconductor is irradiated by ultraviolet (UV) light [6]. The portion of UV in the solar spectrum only accounts for a few percent in the outdoor environment and even lower indoors [7]. The amount of UV in solar radiation greatly reduces the ability of TiO$_2$ to catalyse the oxidations or reductions of harmful compounds into less dangerous ones such as water and carbon dioxide. PC performance can be modified by several different methods including modification of the band gap and doping with additional elements such as transition metals, noble metals and non-metallic elements [8–10]. Coupling the TiO$_2$ with additional structures or compounds such as other semiconductors, organic molecules or oxides can improve PC performance [11–14]. Graphene with its unique electron properties has been combined with TiO$_2$ in several studies to improve performance [15–19]. Some studies have proven that graphene has electron accepting and transport properties that can be successfully used to improve the recombination time in the semiconductor [20].

TiO$_2$ in the form of nanoparticles (NPs) has a widespread use in the improvement of indoor and outdoor air quality [2,21–24]. Poor indoor air quality (IAQ) can be attributed to emission of inorganic pollutants and VOCs from a variety of materials in buildings [25–29], including furnishing, paints, carpets and air fresheners. The presence of various pollutants contribute to sick building syndrome (SBS) [30,31], which is the negative impact of a buildings environment on the life and well-being of its inhabitants.

Among these pollutants, NO$_2$ contributes largely to poor IAQ. This toxic gas is produced from ground-level emissions related to the burning of fossil fuels from vehicles, power plants, industrial sources, and off-road equipment. Several air cleaning technologies have been therefore developed to improve IAQ by reducing NO$_2$ concentration levels [32,33]. PC materials based on TiO$_2$ are the most used for the design of highly efficient systems for environmental reduction of NO$_x$ [34].

Long term exposure to NO$_2$ concentrations higher than those normally found in the ambient air are known to cause an increased risk of acute respiratory illnesses, especially in vulnerable groups. To address concerns associated with NO$_x$ levels the US Environmental Protection Agency (EPA) has set a 1-hour NO$_2$ standard at the level of 100 ppb [35]. Sensors that continuously monitor these low NO$_2$ concentrations in air with the added capability of alerting occupants when NO$_2$ levels have reached harmful levels could be a powerful strategy in the prevention of unacceptable exposure. Both solid electrolyte electrochemical and conductometric sensors are available for detection of NO$_2$ [36–39]. Wide band gap semiconducting metal oxide (MO) based conductometric sensors are commonly used for this purpose, due to their simple functioning, low cost, mass production and easy integration with integrated microelectronic circuits. Among these sensing materials, titania was investigated for developing NO$_2$ sensors [40]. UV- or Vis-light operating TiO$_2$ sensors were also proposed for improving the performance at room to low temperatures and in addition reducing the power consumption of the device [45]. However, the UV- or Vis-light operating TiO$_2$ sensors for room temperature NO$_2$ monitoring so far proposed, do not reach the sensitivity which is needed for environmental applications [41,42].

Owing to the importance of this issue, this paper focuses on the design and preparation of a multifunctional material, with gas sensing and catalytic activity, for the monitoring and abatement of NO$_2$ with the aid of UV- or Vis-light. For this purpose TiO$_2$ and graphene/TiO$_2$ hybrids were synthesized through a simple sol-gel method. As the morphology and microstructure play a fundamental role in both the PC and sensing properties, a detailed characterization has been undertaken. Field emission and conventional scanning electron microscopy (FESEM/SEM), helium ion microscopy (HIM), X-ray diffraction (XRD), BET surface area analysis, differential reflectance spectroscopy, Raman spectroscopy and energy dispersive X-ray analysis (EDX) were used to characterise the physical and chemical properties of both pure TiO$_2$, the hybrid graphene/TiO$_2$ nanoparticles and commercially available

Degussa P25® TiO$_2$ as a reference [43]. As the composition of commercial Degussa P25® is reported to be inhomogeneous between different batches [44], the very same batch was used for all the PC tests in the present work. Then, the PC and sensing properties of synthesized TiO$_2$ and Graphene/TiO$_2$ hybrids were investigated in detail and their performance was correlated with their microstructural characteristics.

2. Experimental

2.1. TiO$_2$ synthesis

Preparation of TiO$_2$ through the sol-gel method is based on the hydrolysis and polymerization of a metal-organic precursor to form a colloidal suspension [45,46]. In the synthesis, 10 ml of tri-tetra-isopropoxide (TTIP) (Sigma Aldrich, ≥ 98%, MM = 284.22; d = 0.96 g/mL) was mixed with 40 mL of 2-propanol (Sigma Aldrich, ≥ 99.7%, d = 0.785 g/mL) in a round bottom flask. The flask, which also acted as the reaction vessel, was positioned above a hotplate/magnetic stirrer within a fume cupboard. A flat crystallizer dish containing the reaction vessel was filled with water thereby ensuring the flask was heated evenly at a temperature of 80 °C A separator funnel was filled with deionized water and adjusted to a pH of 2 using nitric acid measured with an Omega PHB23 pH-meter mounted above the round bottom flask. In the synthesis of undoped TiO$_2$, acidified deionised water was added to the alcoholic solution with the titanium precursor. The acid provided the optimum pH for the hydrolysis reaction.

The 2-propanol and TTIP precursor were mixed under continuous vigorous stirring for 1 h at a temperature of 80 °C before the acidified water was introduced into the reaction vessel at a rate of 2 mL min^{-1} to initiate the hydrolysis reaction. After continuous stirring for 6 h a white coloured colloidal liquid containing 5 g L^{-1} TiO$_2$ was obtained through the reaction described in Eq. (1):

$$Ti[OCH(CH_3)_2]_4 + 2\ H_2O \rightarrow TiO_2 + 4\ (CH_3)_2CHOH \qquad (1)$$
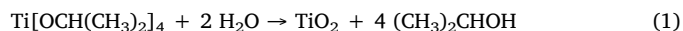
After completion of the reaction all the excess solvent was removed immediately by evaporation through continuous stirring on a hotplate at 80 °C. The TiO$_2$ was initially amorphous and required annealing to form the anatase crystalline phase that exhibits higher PC activity compared to amorphous or rutile TiO$_2$ [47,48]. Annealing was carried out using an Elite BRF 14/10-2416 CG furnace with the material held in an alumina crucible of internal volume 20 ml. The annealing was achieved by ramping the temperature at a rate of 200 °C/h followed by a dwell at 450 °C, for 2.5 h before cooling.

2.2. Graphene/TiO$_2$ sample synthesis

Commercial graphene nanoplatelets, CamGraph® G1, kindly supplied by Cambridge Nanosystems, were used. These were manufactured using a surfactant-free microwave plasma synthesis process. According to the manufacturers analysis these consisted of 3 ± 2 layers and had a surface area of 320 ± 20 m^2/g with a typical elemental analysis of 97.8% carbon, 0.68% hydrogen, 0.29% nitrogen and 0.99% oxygen. A Raman spectrum and XRD pattern of the graphene are presented in Fig. S1a and b (Supplementary Information File). Graphene/TiO$_2$ samples were prepared following two different protocols.

In the first synthesis, graphene was added to the reaction vessel together with the TTIP, equating to 10 wt% of graphene. The mixture was then stirred at 80 °C for 2 h before initiating the hydrolysis reaction with acidified water. A grey colloidal solution was formed, with a pH of 1.8 – measured using an Omega PHB23 pH-meter. Following the completion of the reaction, the sample was recovered, by evaporation of the solvent in the hotplate, and annealed following the procedure described above in the Section 2.1: "TiO$_2$ synthesis" – at 450 °C by ramping at a rate of 200 °C/h and a 2.5 h dwell time at the selected temperature. This material is referred to as **GTiO$_2$S**.
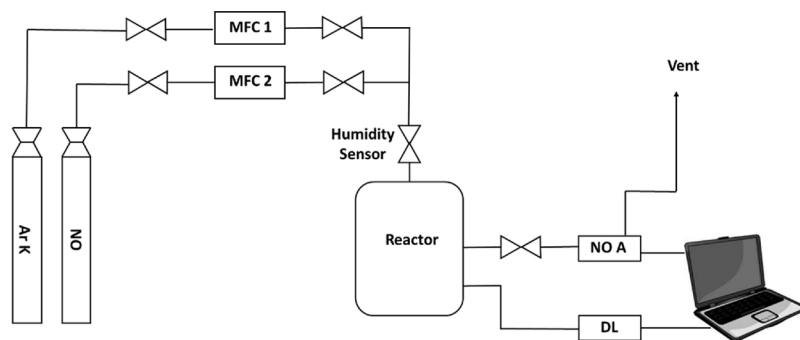
Fig. 1. Scheme of the photocatalytic setup of NO_x degradation. MFC is mass flow controller, **NO A** is the NO analyser and **DL** is the data logger.

In the second procedure, TiO_2 was prepared following the synthesis previously described in Section 2.1 "*TiO_2 synhesis*". It was then placed in a beaker, together with a mixture of ethanol and water (50% wt), and 10% wt of CamGraph graphene. This solution, was stirred at 70 °C for two hours, and then the solvent was removed by evaporation on the hotplate at 80 °C, to collect the powder. As the TiO_2 was annealed prior to the graphene being added, the graphene was not subjected to any heat treatment. This material was named **GTiO₂M**.

2.3. Sample characterization

Analysis using X-ray diffraction (XRD) was carried out to evaluate the weight percentage of crystalline phases in the specimens prepared in addition to microstructural features. Semi-quantitative phase analysis (QPA) of the XRD data was performed using the Rietveld method. Rietveld refinements were assessed using the GSAS-EXPGUI software packages [49,50]. XRD data were collected on a PANalytical X'Pert Pro (NL) θ/θ diffractometer, equipped with a fast real-time multiple strip (RTMS) detector (PIXcel 1D, PANalytical), using Cu K_α radiation (45 kV and 40 mA) with a virtual step size of 0.02°2θ and virtual time per step of 200 s over a 20–80°2θ range. The instrumental broadening was measured using the NIST SRM 660b standard (LaB_6) with data collected under the same conditions as those used for the TiO_2 samples. XRD was also used to determine microstructural features from the specimens. For this purpose, XRD data were collected in the same instrument with identical set-up as that used for QPA analysis. A higher signal-to-noise ratio was achieved in the range of 20–145°2θ, using a virtual step size of 0.1°, and a virtual time per step of 500 s. The instrumental contribution was obtained by parameterising the profile of fourteen (hkl) reflections from the NIST SRM 660b standard (LaB_6), according to the Caglioti et al. relationship [51]. Microstructural features of the specimens were analysed through the whole powder pattern modelling (WPPM) method [52], as implemented in the PM2K software package [53]. By means of this novel methodology, the size distribution of individual phases in NPs can be accurately defined [54]. In this work, crystalline domains were assumed to be spherical, and their diameter distributed according to a log-normal curve.

Raman spectra where acquired using a Renishaw System 2000 spectrometer equipped with an inVia Raman microscope using a He-Ne laser as an excitation source operating at 785 nm and a maximum power of 20 mW. The samples were analysed by focusing the laser with objective magnification ×100 onto the sample surface corresponding to a laser spot diameter of about 10 μm. The acquisition time of 1 s was used for each spectrum over the wavenumber range 100–3500 cm⁻¹ with a 4 cm⁻¹ resolution.

The morphology of the aggregates of TiO_2 and graphene/TiO_2 was studied using a JEOL JSM-6480lv scanning electron microscope (SEM) with Oxford INCA Energy X-ray Analyser correlated using an acceleration voltage of 20 keV. A higher magnification study of the particles using a helium ion microscope (HIM) was obtained using a Zeiss Orion NanoFab instrument. The images were acquired using He⁺ ions with an

accelerating voltage of 25 kV and beam current of 0.3 pA with the angle varied between 0 and 54 deg. Images of higher magnification were obtained using a JEM-2100Plus Transmission Electron Microscope (TEM) using an acceleration voltage of 200 keV and a spot size of 1 nm.

Diffuse reflectance spectroscopy (DRS) was performed with a Shimadzu UV 3100 (JP) spectrometer and spectra of the samples were acquired in the UV–Vis range (250–850 nm), with 0.2 nm step-size, and Spectralon® white reference material. The Kubelka-Munk theory, Eq. (2), was applied to allow conversion of the diffuse reflectance into the pseudo-absorption coefficient α, afterwards, the Tauc plot was used to estimate the electronic transition in the specimens prepared:

$$(\alpha h \nu)^{1/\gamma} = A(h\nu - E_g) \tag{2}$$

where h is Planck's constant, ν is the photon frequency, α is the pseudo-absorption coefficient, E_g is the band gap, and A is a proportionality constant. The value of the power coefficient γ denotes the nature of the electronic transition, whether allowed or forbidden and whether direct or indirect: for direct allowed transitions: $\gamma = 1/2$, while for indirect allowed transitions, $\gamma = 2$ [55]. The specific surface area (SSA) of the prepared samples was determined using the Brunauer–Emmett–Teller (BET) method (Micromeritics Gemini 2380, US), using N_2 as the adsorbate gas.

2.4. NO_x photocatalytic activity

Gas-solid phase PC study was carried out in a reactor operated continuously, as previously described in detail by Lucas et al. [56]. It comprised a cylindrical chamber (~35 L in volume, 70 cm in height, 25 cm in diameter) constructed from a high grade stainless steel with a stainless steel top with a sealed glass window to allow the light to reach the sample that was placed inside. A schematic diagram is shown in Fig. 1, whilst a digital photograph of the working rig is in Fig. S2. The light source employed was a solar lamp (Osram Ultra-Vitalux, 300 W, 280 to 780 nm), placed 65 cm from the photocatalyst. The light intensity reaching the samples, measured with a radiometer (Delta OHM, HD2302.0, IT), was found to be approximately 3.6 W m⁻² in the UV-A range and 25 W m⁻² in the visible-light range. A Petri dish 6 cm in diameter was filled up with a layer of powder. The tests were performed at 27 ± 1 °C (temperature inside the reactor) with a relative humidity (RH) of 31%. These parameters were controlled by means of a thermocouple that was placed inside the chamber and a humidity sensor placed in the inlet pipe and they remained stable throughout the tests. The concentration of the pollutant gas exiting through the outlet was measured using a chemiluminescence analyser (AC-31 M, Environment S.A).

The experiment was conducted by firstly placing the petri dish containing the photocatalyst inside the reactor and covering the glass window with a sheet of aluminium. The inlet gas mixture (prepared mixing gas cylinders containing synthetic air and NO_x) was allowed to flow into the chamber until it stabilized at a concentration of 200 ppb. The mixture of air with that concentration of NO_x was guaranteed using

two mass flow controllers with a flow rate of 1 L min^{-1}. The condition of continuous flow was necessary to achieve sample saturation, ensuring that, during the test, the PC process was the only one involved (*i.e.*, no absorption from the sample, nor from the reactor walls) [57]. Once a concentration of 0.2 ppm was reached, the window glass was un-covered, the lamp turned on, and the PC reaction started. When the pollutant concentration stabilized to a minimum concentration the NO$_x$ was no longer being decomposed by the catalyst. The PC efficiency was then expressed in terms of the conversion rate (%) of the initial NO$_x$ concentration which was calculated using Eq. (3) [58]:

$$(NO_x\ conversion)\ \% = \frac{(NO_x)_0 - (NO_x)_t}{(NO_x)_0} \times 100 \tag{3}$$

where $(NO_x)_0$ and $(NO_x)_t$ are the initial and final concentrations (both expressed as ppb) after an irradiation time, t.

2.5. NO₂ sensing tests

NO$_2$ sensing tests were carried out on conductometric platforms fabricated using alumina substrates (3 × 6 mm), supplied with inter-digitated Pt electrodes and a heating element on the back side. Printable pastes of sensitive materials were obtained mixing TiO$_2$ based samples with distilled water, then each paste was screen printed onto the interdigitated electrodes to obtain a thick film (∼ 10 μm) with a sensitive geometrical area of 3 × 3 mm. The high porosity of the alu-mina meant that no binder was necessary to enhance the adhesion of the sensing layer on the alumina substrate.

All measurements were performed at room temperature (RT) in a 10 ml volume test chamber equipped with a 400 nm UV–vis low power LED (180 mW) [59,60]. For the entire duration of the measurement, the sensor was exposed to a constant synthetic air total stream of 100 sccm (standard cubic centimeters per minute) with a RH of about 40%. The resistance of the sensors was monitored using a Keithley 6487 Pi-coammeter at an applied voltage of 1 V. The sensing tests under UV excitation were performed exposing the sensor to the target gas while the sensitive film was constantly irradiated with the UV light. The gas response was defined as the ratio $S = R_0/R$, where R_0 represents the electrical resistance of the sensor in air and R is the electrical resistance of the sensor at a given NO$_2$ concentration.

3. Results and discussion

3.1. Morphological characterization

SEM, HIM and TEM images were acquired to investigate the mor-phology of the synthesized powder. Fig. 2a shows a low magnification image of one of large aggregates observed on the pure TiO$_2$ sample. The rough surface of TiO$_2$ aggregates, consisting of nanoparticles around 20 nm ± 5 nm, is clearly observed at high magnification (Fig. 2b). TEM analysis confirmed the nanometric size of TiO$_2$ particles and their aggregation even at nanometer level (Fig. 2c and d).

Electron microscopy of the **GTiO₂S** sample is reported in Fig. 3. The presence of graphene in the **GTiO₂S** modified the nucleation and growth of TiO$_2$ aggregates as shown in Fig. 3a. The dimension of the particles measured in post processing does not change significantly when compared with pure TiO$_2$. Fig. 3c) shows how graphene sheets behave as a nucleation point for the titania. Fig. 3d) focuses on the interface between the graphene sheet and the TiO$_2$ NPs.

Fig. 4a) and b) show the intricate network of TiO$_2$ and graphene in the **GTiO₂M** sample that was not observed in the **GTiO₂S** sample. Graphene and TiO$_2$ are deeply embedded together, and this modified the shape and the roughness of the surface of this sample. TEM images were in agreement with those obtained by HIM: Fig. 4c) highlights the intricate network of graphene and TiO$_2$ produced through the mixing of the two components in alcoholic solution. Fig. 4d) shows the interface between TiO$_2$, where atomic lattice planes are visible, and graphene,

where atomic planes are visible.

3.2. Microstructural characterization

XRD patterns of the samples are reported in Fig. 5, while an example of the Rietveld refinement is depicted in Fig. S3. The agreement factors of the Rietveld refinements are reported in Table S1 in addition to the semi-QPA analyses data. The main microstructural features of the specimens are listed in Table 1. In these analyses, only the crystalline TiO$_2$ polymorphs were considered. The sol-gel synthesis of the un-modified **TiO₂** specimen led to the formation of anatase (64.1 wt%) and brookite (35.9 wt%) TiO$_2$ polymorphs. This is in agreement with pre-vious research as anatase is the thermodynamically stable TiO$_2$ poly-morph at the nanoscale [61]. Furthermore, the presence of brookite is to be expected, as it is a common product of such sol–gel syntheses [62,63]. The specimen **GTiO₂M**, quite obviously, had virtually the same mineralogical composition as the unmodified **TiO₂**, *cf* Table 1. On the other hand, the specimen **GTiO₂S** contained slightly less anatase, 57.6 wt%, in favour of a higher amount of brookite, *i.e.* 42.4 wt%. P25$^{\textregistered}$ is composed of 76.3 wt% anatase, 10.6 wt% rutile, and 13.0 wt% amorphous phase as showed by Tobaldi et al. [43].

Microstructural information in the form of the size, and size dis-tribution of anatase and brookite NPs in the specimens was determined using X-ray methods (*cf* Table 1). Quantitative figures are reported in Table S2 and S3 and Fig. 6. Anatase unit cell parameters of **TiO₂** and **GTiO₂M** are virtually the same, as shown in Table S2; the change in the synthesis method (specimen **GTiO₂S**), led to a slight expansion of the anatase *c*-axis, although the unit cell volume is the same in all the three synthesised samples. As per the brookite unit cell parameters these are, once again, virtually the same – within the experimental error – in samples **TiO₂** and **GTiO₂M**. Mixing graphene to the sol, led also in this case to a slight expansion of brookite unit cell volume. Similar ob-servations can be made by considering the average diameter of the anatase crystalline domains in specimens **TiO₂** and **GTiO₂M**. They are virtually the same, within experimental error, being 6.4 and 7.0 nm, respectively, see Table S3 and Fig. 6. Similarly to observations for the unit cell parameters, **GTiO₂S** had a bigger average diameter, being 8.9 nm.

There is no trend for the brookite in the specimens, the average diameter of the crystalline domains being 7.2, 8.8, and 6.2 nm for the **TiO₂**, **GTiO₂M**, and **GTiO₂S** respectively. All the size distributions for brookite had a positive skewness, as shown in Fig. 6.

Raman spectra were obtained to determine the crystalline phase of TiO$_2$ and to allow a comparison with the commercial sample. Fig. S4a shows the Raman spectrum of pure synthesised **TiO₂** showing the presence of anatase and brookite TiO$_2$ polymorphs, thus confirming results from X-ray diffraction. The presence of anatase in crystalline form is indicated by the presence of its characteristic bands at 144, 197, 399, 519 and 639 cm^{-1}; the main brookite Raman modes were detected at: 247, 323, 366 cm^{-1} (*cf* Figure S4a). A Raman spectrum obtained from a sample of **P25** is reported in Fig. S4b. Anatase, rutile and brookite Raman modes are listed in Table S4 [64]. Raman spectra of the hybrid samples containing graphene are reported in Fig. 7. Both spectra indicate the same bands found in the pure synthesised sample attrib-uted to anatase and brookite. Furthermore, the major bands assigned to graphene (*i.e. D* and a weak *D′* band, together with the *G* band) are present in the samples. The presence of these Raman features, *e.g. D* and *D′* bands, is an indication of irregular edge disorders and oxidised dangling bonds [65,66]. Furthermore, as they are with essentially the same intensities, this shows that the defect state in graphene virtually didn't vary between the two synthesis methods employed. Moreover, those defects might have acted as nucleation sites for TiO$_2$ [67].

DRS spectra (not shown) consisted of one single absorption edge, located at around 380 nm, and assigned to the band-to-band transition in titania [68]. The apparent optical E_g of the specimens were calcu-lated by means of the Tauc plot, assuming both a direct allowed and
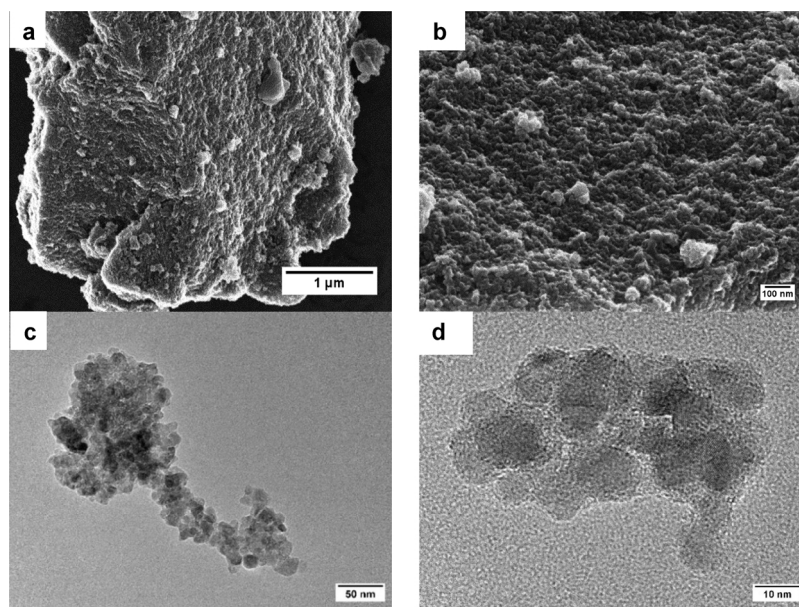
Fig. 2. a) HIM image of TiO$_2$ aggregate, b) HIM image close up of the rough surface of TiO$_2$; c) TEM image of TiO$_2$ nanoparticle aggregate in TiO$_2$ pure; d) high magnification TEM picture of the surface of a small aggregate TiO$_2$ pure particle.

indirect allowed transitions – values listed in Table 1. The E_g values obtained, assuming a direct allowed transition (*cf* Fig. 8), agree well with the expected E_g of anatase (*i.e.* ~ 3.2 eV; ~ 388 nm) reported in the literature [47], thus the direct allowed model would seem more applicable for these specimens. However, the E_g values extracted with the Tauc formalism are shifted toward higher energies compared with the expected E_g value of anatase. This might be a contribution from the non-negligible amounts of brookite in all the specimens. Indeed, the optical band gap of brookite has been reported to be ~ 3.4 eV (~ 365 nm) [69], probably explaining the higher blue-shift of the specimen GTiO2S, which is the specimen with the higher amount of brookite (cf Table 1).Furthermore, although anatase is commonly reported to be a semiconductor having an indirect allowed transition

[70], it has been shown by Serpone and co-workers that, for indirect band gap semiconductors such as anatase, a direct transition might appear, when in a colloidal nanomaterial form [71]. Besides, the presence of graphene did not significantly change the apparent optical E_g, as shown in Table 1.

With regard to the structural properties, an increase in the BET specific surface area of the samples was noted, being 79.6, 87.9, and 100.3 m^2 g^{-1} for the **TiO$_2$**, **GTiO$_2$M**, and **GTiO$_2$S** respectively as reported in Table 1. The sorption isotherms are shown in Fig. S5a–c. They all are of type IV, typical of a mesoporous material. Furthermore, we detected the presence of no micropores (all the pore being in the range of ~ 2-25 nm, inset of Fig. S5a–c). The main microstructural and optical characteristics of the as prepared samples, which are of primary
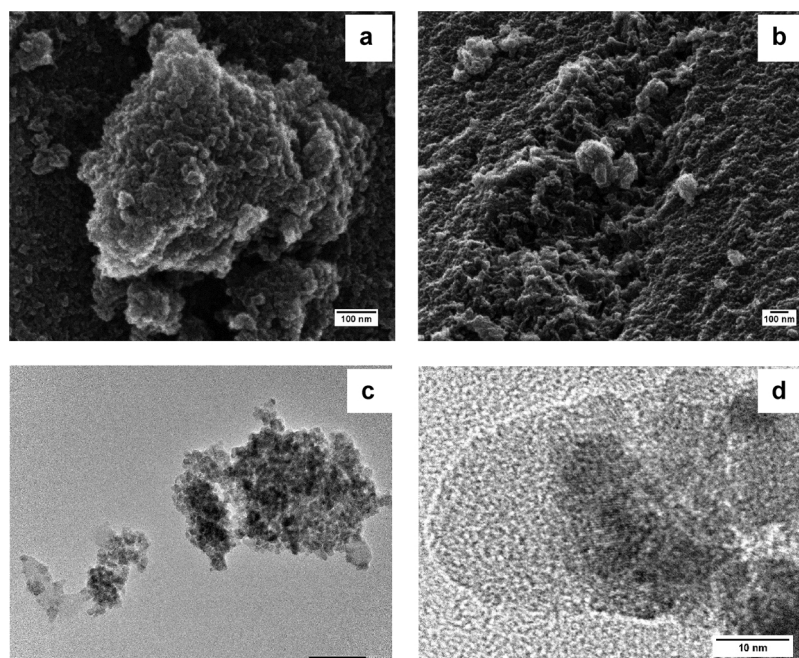

Fig. 3. HIM of **GTiO$_2$S**: a) surface; b) close up of the rough surface. c) TEM image of a TiO$_2$ nanoparticle aggregate anchored to graphene sheets decorated with **GTiO$_2$S**. d) high magnification TEM picture of the interface of atomic planes of TiO$_2$/Graphene in **GTiO$_2$S** particle.
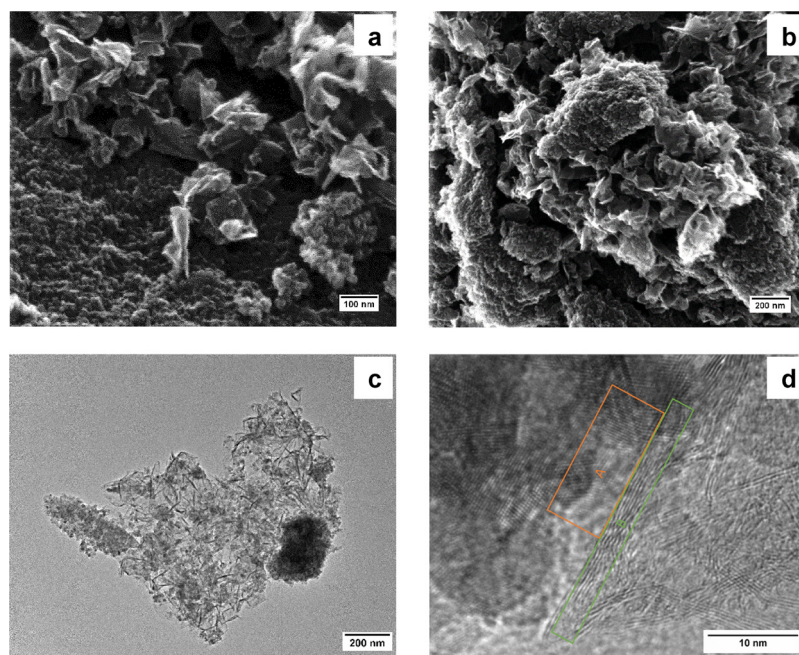
Fig. 4. SEM images of **GTiO₂M** showing a) graphene sheets; b) mixture of graphene and TiO₂. TEM images showing c) graphene sheets decorated with TiO₂ nanoparticles; d) high magnification of the interface of atomic planes of TiO₂ [A box] and graphene planes [B box].
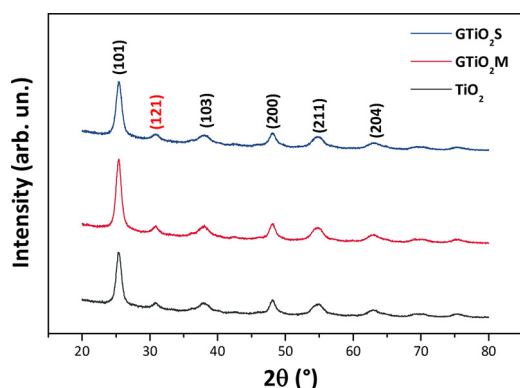

Fig. 5. XRD patterns, from top to bottom, of **GTiO₂S**, **GTiO₂M** and **TiO₂**. Miller indices in black belong to anatase reflections; that in red belongs to brookite.

Fig. 6. Crystalline domain size distribution for a) anatase and b) brookite, in the synthesised specimens.

importance in determining their sensing and PC performances, have also been summarised in Table 1.

3.3. NO₂ sensing tests

TiO₂ is a widely used gas sensor material which can be activated under light. However, so far, only very few TiO₂ based photo-activated sensors have been studied. Furthermore, the range of concentrations investigated is higher than that required for environmental control. Here, the sensing characteristics of the fabricated conductometric sensors have been tested for NO₂ at room temperature in the concentration
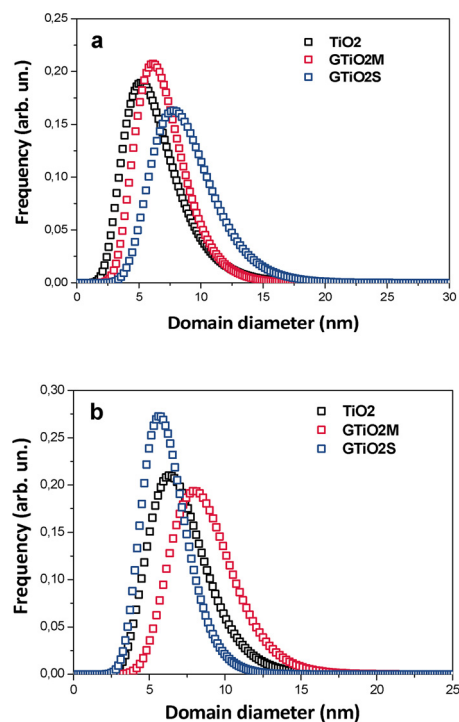
Table 1
Main microstructural and optical characteristics of the as prepared samples.

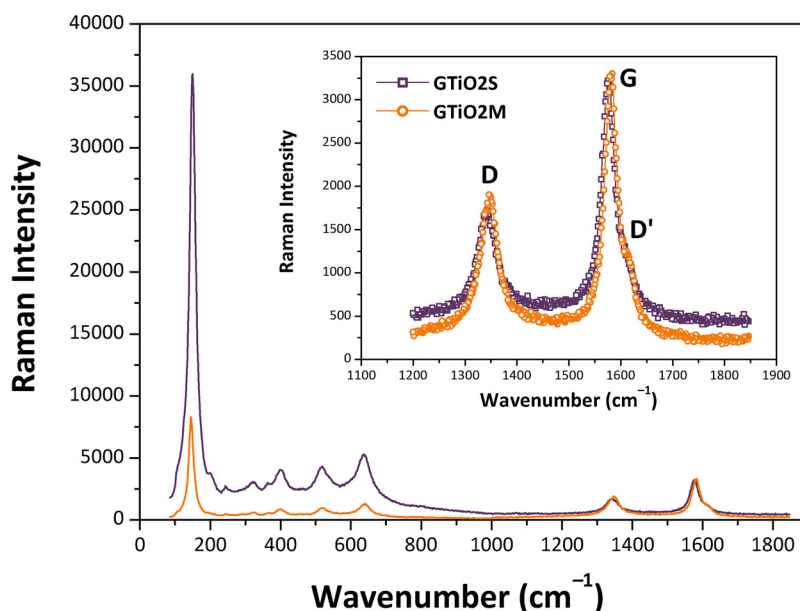| Sample	Phase composition (wt%)		Average domain diameter (nm)		Direct optical band gap		Indirect optical band gap		S_{BET} (m² g⁻¹)
	anatase	brookite	anatase	brookite	eV	nm	eV	nm	
TiO₂	64.1 ± 0.3	35.9 ± 1.0	6.4 ± 0.2	7.2 ± 0.4	3.31	375	2.95	420	79.6 ± 1.1
GTiO₂S	57.6 ± 0.3	42.4 ± 1.1	8.9 ± 0.5	6.2 ± 0.2	**3.35**	**370**	3.06	405	100.3 ± 1.6
GTiO₂M	63.7 ± 0.2	36.3 ± 0.9	7.0 ± 0.5	8.8 ± 0.3	**3.31**	**375**	2.96	419	87.9 ± 1.5

Fig. 7. Raman spectra of **GTiO₂M** and **GTiO₂S**. Inset shows the magnified wavenumber region 1200–1850 cm⁻¹ to highlight the major graphene bands, **D** ($\sim$1350 cm⁻¹), **D′** (around 1620 cm⁻¹), and **G** (1580 cm⁻¹).
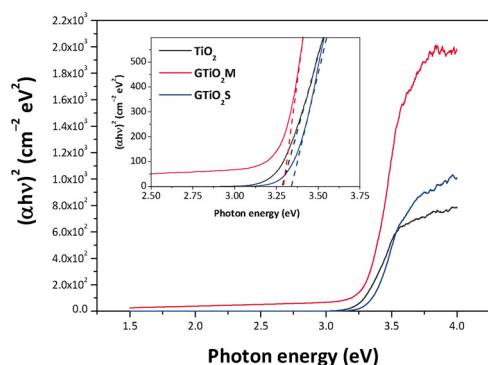

Fig. 8. Kubelka–Munk analysis of the DRS data *versus* photon energy of the specimens to show the optical E_g, calculated using the Tauc procedure. In the inset, the dotted lines represent the *x*-axis intercept of the line tangent to the inflection point of the sample, *i.e.* the optical E_g according to the direct allowed E_g model – $(\alpha h\nu)^2$, $\gamma = \frac{1}{2}$.

Fig. 9. Effect of the UV–vis excitation on the response behaviour of the a) unmodified **TiO₂** and b) **GTiO₂S** sensor toward NO₂ (1750 ppb) at 40% RH.

range from 70 ppb to 1750 ppb. Notably, to reduce the size and the power consumption of the photo-activated sensors, a low-power light emitting diode (LED) lamp (180 mW) was used. LEDs are promising for gas sensing applications because of their reduced size, instant on/off operation, long lifetime, low environmentally impact and ability to produce accurate wavelengths at specific intensities.

Preliminary tests, carried out to investigate the effect of the UV–vis excitation on the behaviour of the pure **TiO₂** and **GTiO₂S** sensors toward NO₂ (1750 ppb), are shown in Fig. 9. In the dark, almost no difference in the sensor response is noted. Looking at the sensor response under UV–vis excitation with a 400 nm LED, no appreciable variation occurs for the unmodified **TiO₂** sensor, whereas the **GTiO₂S** sensor shows a two-fold increase in response. It worth noting that, under UV–vis excitation a quick and reversible recovery of the baseline was observed for both sensors.

The positive response of the synthesized TiO₂ and graphene/TiO₂ hybrids under UV excitation for different concentrations of NO₂ and the related calibration curves, are reported in Fig. 10. To make the comparison clearer, both the data sets have been plotted on the same scale. Both **TiO₂** and **GTiO₂S** based sensors showed changes in resistance when exposed to NO₂ in the range 70–1750 ppb. On the contrary, the
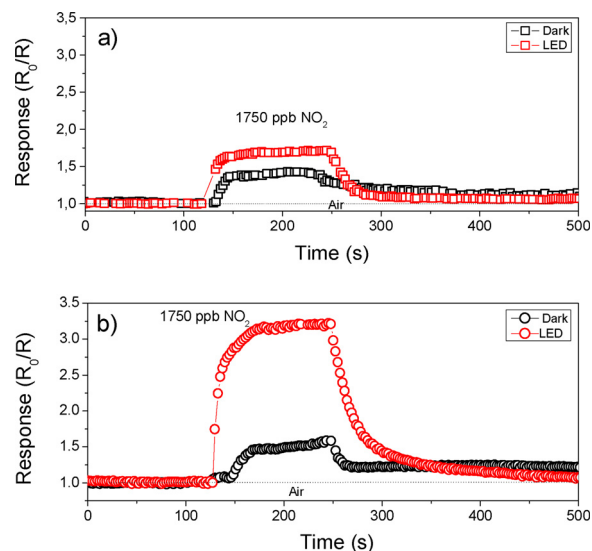
GTiO₂M based sensor was almost insensitive to NO₂ in the same range of concentration. This may be due to the high conductivity of the sample, through the well-interconnected graphene sheets which promote electronic transport. A decrease in the resistance has been clearly observed after the introduction of NO₂ (Fig. 10a and b). As NO₂ is an oxidizing gas, this suggests that the tested materials behave as *p*-type semiconductors. Such behaviour can be explained assuming that NO₂ adsorption on the titania active layers involves the transfer of electrons toward the titania sensing layer, decreasing the resistance of the sensor device.

Fig. 10c compares the response under UV excitation to 1750 ppb of NO₂ of the synthesized TiO₂ and graphene/TiO₂ hybrid-based sensors. The results, summarised in Fig. 10d at different concentrations indicate that the **GTiO₂S** sensor was the most responsive, in agreement with previous behaviour of TiO₂-based sensors reported in the literature [41,72]. The calibration curve for the **GTiO₂S** sensor reported in log-log scale (see Fig. 11) has a good linear relationship ($R^2 = 0.984$) according
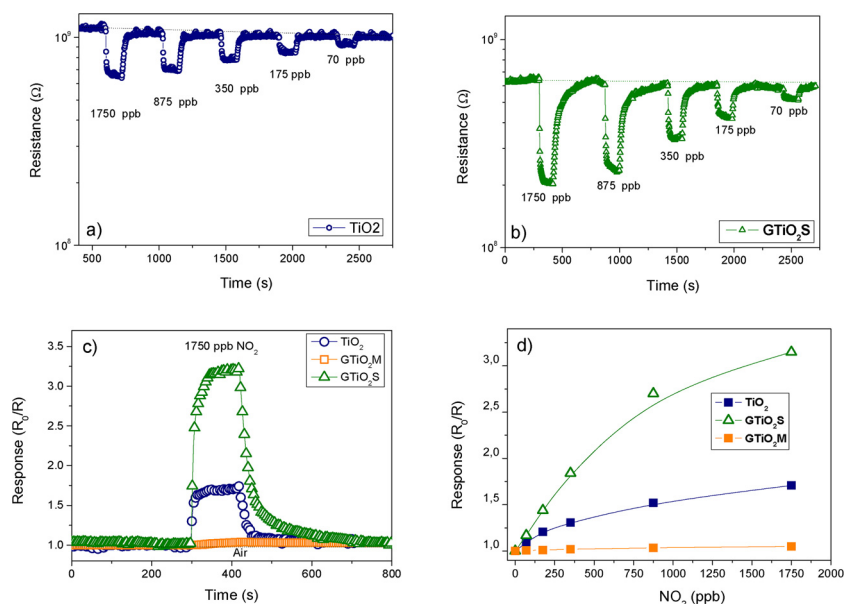
Fig. 10. Resistance variation under UV excitation for: a) the unmodified **TiO₂** and b) **GTiO₂S** at different concentration of NO₂. c) Comparison of the response of the synthesized TiO₂ and TiO₂/graphene/ hybrids; d) Calibration curves.
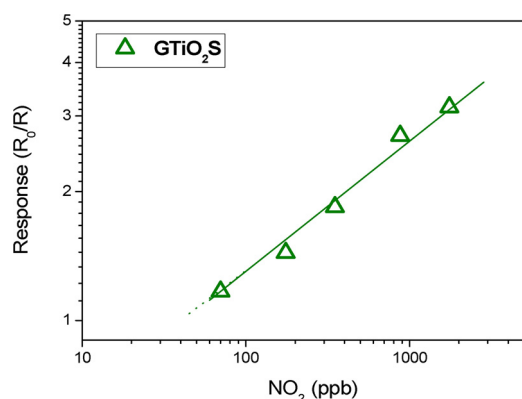

Fig. 11. Calibration curve of the **GTiO₂S** sensor in log-log format.
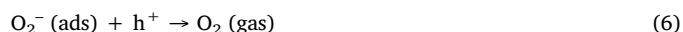
to Eq. (4):

$$logS = 0.33 \cdot logc - 0.54 \qquad (4)$$

where S is the response (R_0/R) and c the concentration of NO₂. The limit of detection (LOD) estimated at a signal to noise ratio of 3, was found to be about 50 ppb of NO₂.

The gas sensing performances of the **GTiO₂S** sensor are compared in Table 2 with previously reported TiO₂-based NO₂ sensors. It is noteworthy that almost all TiO₂ sensors work at high temperature and only in the ppm range of concentration. In comparison the proposed GTiO2S sensor tested in this work possesses a lower operating range of concentration up to ppb level, functioning at room temperature, with a comparable or superior response to the other TiO2-based formulations with a relatively short response/recovery time.

The data reported above can help to propose a plausible mechanism for the enhanced response in the presence of UV–vis light. It is well known that light irradiation of the sensing layer affects gas detection in metal oxide semiconductors, enhancing the carrier generation. In addition, it is also responsible for the photo-dissociation of the target gas [59]. The results obtained, indicated that the resistance of TiO₂ decreased upon exposure to NO₂ and decreased further with LED excitation, increasing the response. This occurs through the combination of processes reported below, starting with the photo-generation of electron-hole pairs (Eq. 5). The photo-generated holes react with adsorbed

oxygen ions, forming O₂ (gas) which leaves the sensing surface (Eq. 6). Adsorption of NO₂ target gas is then enhanced on the clean and more reactive surface. Removal of oxygen contamination from the illuminated surface results in a greater formation of reactive sites for NO₂ adsorption. The photo-induced adsorption of NO₂ has been suggested to be the key pathway for higher response [79,80]. Adsorbed NO₂ extracts electrons from the conduction band (Eq. (7)), increasing the number of holes in *p*-type TiO₂ and consequently decreasing the resistance.

$$TiO_2/graphene + h\nu \rightarrow h^+ + e^- \qquad (5)$$

$$O_2^- (ads) + h^+ \rightarrow O_2 (gas) \qquad (6)$$

$$NO_2 (gas) + e^- \rightarrow NO_2^- (ads) \qquad (7)$$

In summary, due to the increased availability of NO₂ molecules adsorbed, the resistance change upon exposure to NO₂ under photoexcitation was higher than in the dark. The substantial enhancement in the response of the **GTiO₂S** sensor to NO₂ gas under the LED excitation compared to the other samples was attributed to its higher surface area (smaller particle size).

3.4. Photo-catalytic NOₓ degradation tests

Results of NOₓ PC degradation using the solar lamp are shown in Fig. 12. All the specimens exhibited PC activity when triggered with a lamp simulating solar radiation. Graphene modified TiO₂ specimens were the most active amongst the whole series of samples, with **GTiO₂S** being more active than **GTiO₂M**. On the other hand, **P25°** is more photocatalytically active than our unmodified **TiO₂** sample.

These results are well confirmed by the initial (first 20 min of reaction) pseudo-first order kinetic constants, *cf* Fig. 13, in which are reported the values averaged over three consecutive PC activity tests (using the same specimen as in the first PC run) with the respective standard deviation. These data are supported by the literature which states that graphene is a high performance support for photocatalysis [81]. Thus, because electronic transport is enhanced in the graphene/TiO₂ hybrids, as shown in Section 3.3, a decrease in the resistance of **GTiO₂S**, improves PC activity. The photo-generated electrons, from the TiO₂ component, are swiftly delivered to the surrounding graphene sheets in a composite process [82]. Such electrons are involved in reductive reactions, *i.e.* the formation of active O₂⁻ species with the

Table 2
Gas sensing performances of TiO_2-based NO_2 sensors.

| Material	Operating temperature (°C)	Concentration range (ppm)	Response	Response /recovery times (s)	Ref.
TiO_2 nanoparticles	500	2–25	R_{NO2}/R_{N2} 2.3–5.1	90–150	[73]
TiO_2 nanorods/ nanoparticles	300/UV	1–10	I_{air}/I_{NO2} 8–45	–/–	[74]
TiO_2 nano-tubular	400	10–100	R_{NO2}/R_{Ar} 4.3–7.7	360/300	[40]
Al-TiO_2	600	50–200	R_{NO2}/R_{Ar} 1.8–3.5	180/720	[75]
ZnO–TiO_2 nanocomposite	250	2–20	$\Delta R/R_{air}\%$ 4–57	120/113	[76]
Cr-TiO_2 nanotubular	500	10–100	R_{air}/R_{NO2} 3.2–12.2	180/360	[77]
TiO_2 thin film	RT/UV	100–500	$\Delta R/R_{air}\%$ 1.3–2.2	100/210	[41]
TiO_2 nanowires	RT	10–100	R_{air}/R_{NO2} 2.4–3.1	10/19	[78]
TiO_2/graphene	RT/UV	0.07–1.75	R_{NO2}/R_{Air} 1.17–3.14	35/90	**This work**
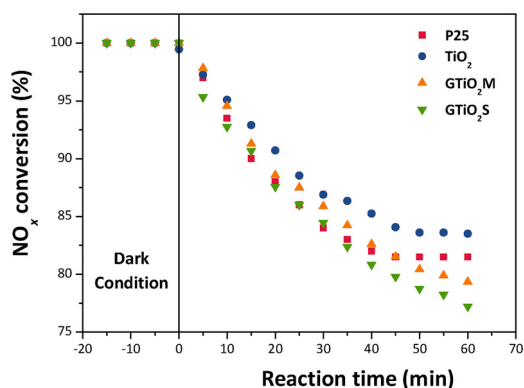
Fig. 12. NO_x degradation graph of all the samples irradiated with OSRAM solar lamp. The initial negative time zone indicates a period of stabilization of the chamber; positive time indicates that the light has been turned on starting the experiment.
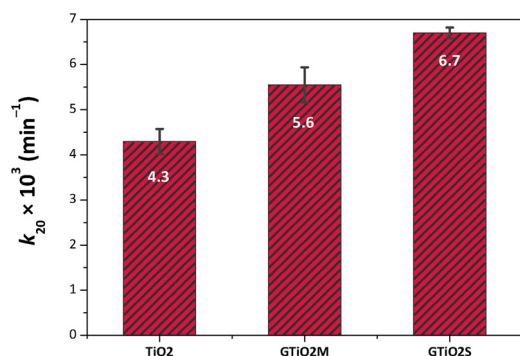

Fig. 13. Histograms showing the initial (first 20 min of reaction) pseudo-first order kinetic constants, k'_{app}. Reported values are averaged over three consecutive photocatalytic activity tests.

oxygen from the environment, as in Eq. (8) [83]. Furthermore, and most importantly for PC purposes, the removal of these electrons from TiO_2 to graphene, allows for a boost in the separation of the photo-generated pair [84]. Moreover, the incorporation of TiO_2 on a graphene substrate is able, at the same time, to increase the adsorption of pollutants [85], all these factors being beneficial for PC activity.

However, data also show that there is a clear difference in the interaction amongst TiO_2 NPs and graphene, depending on the preparation method. Consistent with the sensing experiments, **GTiO₂S** behaves

itself as the best performing sample in the PC tests despite the thermal treatment that was necessary after the preparation of the specimen. Indeed, such a thermal treatment might be beneficial in synthesising TiO_2 and graphene in more intimate contact (*cf* Fig. 3d); furthermore, the introduction of graphene directly into the sol was beneficial in producing NPs with a higher SSA, as shown in Table 1. Also, as shown by Trapalis and co-workers [84], the photocatalytic de-NO_x performance of graphene-TiO_2 composites reaches a maximum efficiency at low graphene loadings. This was attributed by those authors to the interaction between TiO_2 nanoparticles and graphene sheets, acting as electron traps.

Plotting the degradation of NO and NO_2 *versus* reaction time of **GTiO₂S**, Fig. 14, the concentration of NO_2, after having turned the lamp on, is virtually stable, whilst NO concentration is degraded. Consequently, Eqs. (5,8–10) may be involved in the oxidative reaction processes [86]:

$$e_{CB}^- + O_{2(ads)} \rightarrow {}^{\cdot}O_{2(ads)}^- \qquad (8)$$

$$NO + {}^{\cdot}O_{2(ads)}^- \rightarrow NO_3^- \qquad (9)$$

$$NO_3^- + H^+ \rightarrow HNO_3 \qquad (10)$$

This observation is consistent with previous literature where Dong and colleagues (*via* electron spin resonance) have shown that super-oxide radicals (${}^{\cdot}O_2{}^-$) are the main active reactive oxygen species responsible for the PC degradation of NO_x [87], thus we can state that NO was mainly oxidised by oxygen radicals. Finally, it is well known that HNO_3 is the final product of the NO_x degradation. However, as shown
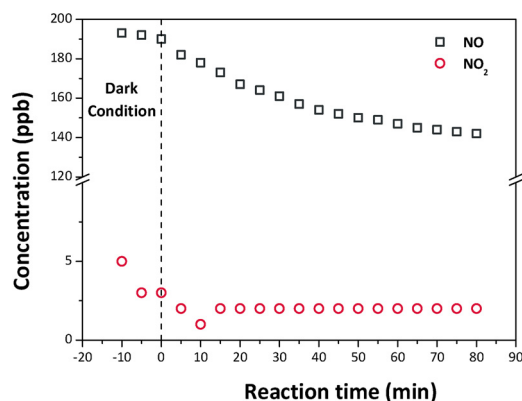

Fig. 14. Concentration of NO and NO_2 *versus* irradiation time, specimen **GTiO₂S**.

by Ohko and colleagues, this can be easily eluted from the catalyst into water [88].

4. Conclusions

A sol gel synthesis has been used to synthesize graphene/TiO$_2$ nanoparticles. Addition of graphene to the reaction vessel prior to initiating the sol gel reaction, followed by annealing, led to an intimately mixed composite (**GTiO$_2$S**). An alternative manufacturing method involving the addition of graphene to TiO$_2$ nanoparticles which had already been annealed resulted in a material with lower performance (**GTiO$_2$M**). XRD and Raman data were complementary in describing the different structures observed. The as-prepared samples were evaluated as sensing materials for monitoring NO$_2$ at low concentrations in air. Under UV–vis photo-excitation, the **GTiO$_2$S** sensor was the most responsive. The significant improvement in sensitivity at room temperature under the UV–vis excitation was attributed to higher surface area (smaller particle size) compared to the other samples. The physical mechanisms, *i.e.* the photo-generation of free charge carriers and the resulting reactions between semiconductor surface and oxygen and NO$_2$ are likely under LED excitation. Interestingly, the PC properties which result in the abatement of NO$_x$ follow the same trend seen in NO$_x$ sensing, with **GTiO$_2$S** being the most active material when compared to both **GTiO$_2$M** and **TiO$_2$ pure,** making it the most suitable for multipurpose environmental applications.

Conflict of interest

No conflicts of interest.

Acknowledgments

Appendix A. Supplementary data

Supplementary material related to this article can be found, in the online version, at doi:https://doi.org/10.1016/j.apcatb.2018.10.032.

References

[1] A. Fujishima, K. Honda, Electrochemical photolysis of water at a semiconductor electrode, Nature 238 (1972) 37–38, https://doi.org/10.1038/238037a0.

[2] C.H. Ao, S.C. Lee, Indoor air purification by photocatalyst TiO$_2$ immobilized on an activated carbon filter installed in an air cleaner, Chem. Eng. Sci. 60 (2005) 103–109, https://doi.org/10.1016/j.ces.2004.01.073.

[3] Y. Paz, Application of TiO$_2$ photocatalysis for air treatment: patents' overview, Appl. Catal. B Environ. 99 (2010) 448–460, https://doi.org/10.1016/j.apcatb.2010.05.011.

[4] M. Hussain, N. Russo, G. Saracco, Photocatalytic abatement of VOCs by novel optimized TiO$_2$ nanoparticles, Chem. Eng. J. 166 (2011) 138–149, https://doi.org/10.1016/j.cej.2010.10.040.

[5] S. MiarAlipour, D. Friedmann, J. Scott, R. Amal, TiO$_2$/porous adsorbents: recent advances and novel applications, J. Hazard. Mater. 341 (2018) 404–423, https://doi.org/10.1016/j.jhazmat.2017.07.070.

[6] M. Landmann, E. Rauls, W.G. Schmidt, The electronic structure and optical response of rutile, anatase and brookite TiO$_2$, J. Phys. Condens. Matter 24 (2012) 195503, , https://doi.org/10.1088/0953-8984/24/19/195503.

[7] B.L. Diffey, Sources and measurement of ultraviolet radiation, Methods 28 (2002) 4–13, https://doi.org/10.1016/S1046-2023(02)00204-9.

[8] W.-J. Yin, S. Chen, J.-H. Yang, X.-G. Gong, Y. Yan, S.-H. Wei, Effective band gap narrowing of anatase TiO$_2$ by strain along a soft crystal direction, Appl. Phys. Lett. 96 (2010), https://doi.org/10.1063/1.3430005 221901.

[9] R. Long, N.J. English, Band gap engineering of double- cation -impurity-doped anatase-titania for visible-light photocatalysts: a hybrid density functional theory approach, Phys. Chem. Chem. Phys. 13 (2011) 13698–13703, https://doi.org/10.1039/C1CP21454C.

[10] S.G. Kumar, L.G. Devi, Review on modified TiO$_2$ photocatalysis under UV/Visible light: selected results and related mechanisms on interfacial charge carrier transfer dynamics, J. Phys. Chem. A 115 (2011) 13211–13241, https://doi.org/10.1021/jp204364a.

[11] J. Godnjavec, J. Zabret, B. Znoj, S. Skale, N. Veronovski, P. Venturini, Investigation of surface modification of rutile TiO$_2$ nanoparticles with SiO$_2$/Al$_2$O$_3$ on the properties of polyacrylic composite coating, Prog. Org. Coat. 77 (2014) 47–52, https://doi.org/10.1016/j.porgcoat.2013.08.001.

[12] S. Ke, X. Cheng, Q. Wang, Y. Wang, Z. Pan, Preparation of a photocatalytic TiO$_2$/ZnTiO$_3$ coating on glazed ceramic tiles, Ceram. Int. 40 (2014) 8891–8895, https://doi.org/10.1016/j.ceramint.2014.01.027.

[13] R. Phienluphon, K. Pinkaew, G. Yang, J. Li, Q. Wei, Y. Yoneyama, T. Vitidsant, N. Tsubaki, Designing core (Cu/ZnO/Al$_2$O$_3$)–shell (SAPO-11) zeolite capsule catalyst with a facile physical way for dimethyl ether direct synthesis from syngas, Chem. Eng. J. 270 (2015) 605–611, https://doi.org/10.1016/j.cej.2015.02.071.

[14] Z. Li, Y. Hou, B. Ma, X. Wu, Z. Xing, K. Li, Super-hydrophilic porous TiO2-ZnO composite thin films without light irradiation, Environ. Prog. Sustain. Energy 35 (2016) 1121–1124, https://doi.org/10.1002/ep.12308.

[15] Y. Yao, G. Li, S. Ciston, R.M. Lueptow, K.A. Gray, Photoreactive TiO$_2$/carbon nanotube composites: synthesis and reactivity, Environ. Sci. Technol. 42 (2008) 4952–4957, https://doi.org/10.1021/es800191n.

[16] Y.-J. Xu, Y. Zhuang, X. Fu, New insight for enhanced photocatalytic activity of TiO$_2$ by doping carbon nanotubes: a case study on degradation of benzene and methyl orange, J. Phys. Chem. C 114 (2010) 2669–2676, https://doi.org/10.1021/jp909855p.

[17] Y. Liang, H. Wang, H. Sanchez Casalongue, Z. Chen, H. Dai, TiO$_2$ nanocrystals grown on graphene as advanced photocatalytic hybrid materials, Nano Res. 3 (2010) 701–705, https://doi.org/10.1007/s12274-010-0033-5.

[18] Y. Zhang, Z.-R. Tang, X. Fu, Y.-J. Xu, TiO$_2$−graphene nanocomposites for gas-phase photocatalytic degradation of volatile aromatic pollutant: is TiO$_2$−graphene truly different from other TiO$_2$−carbon composite materials? ACS Nano 4 (2010) 7303–7314, https://doi.org/10.1021/nn1024219.

[19] J. Liu, H. Bai, Y. Wang, Z. Liu, X. Zhang, D.D. Sun, Self-assembling TiO$_2$ nanorods on large graphene oxide sheets at a two-phase interface and their anti-recombination in photocatalytic applications, Adv. Funct. Mater. 20 (2010) 4175–4181, https://doi.org/10.1002/adfm.201001391.

[20] K. Zhou, Y. Zhu, X. Yang, X. Jiang, C. Li, Preparation of graphene–TiO$_2$ composites with enhanced photocatalytic activity, New J. Chem. 35 (2011) 353–359, https://doi.org/10.1039/C0NJ00623H.

[21] J. Auvinen, L. Wirtanen, The influence of photocatalytic interior paints on indoor air quality, Atmos. Environ. 42 (2008) 4101–4112, https://doi.org/10.1016/j.atmosenv.2008.01.031.

[22] M. Nuño, R.J. Ball, C.R. Bowen, Study of solid/gas phase photocatalytic reactions by electron ionization mass spectrometry: study of photoreactions by mass spectrometry, J. Mass Spectrom. 49 (2014) 716–726, https://doi.org/10.1002/jms.3396.

[23] M. Nuño, R.J. Ball, C.R. Bowen, R. Kurchania, G.D. Sharma, Photocatalytic activity of electrophoretically deposited (EPD) TiO$_2$ coatings, J. Mater. Sci. 50 (2015) 4822–4835, https://doi.org/10.1007/s10853-015-9022-0.

[24] M. Nuño, G.L. Pesce, C.R. Bowen, P. Xenophontos, R.J. Ball, Environmental performance of nano-structured Ca(OH)$_2$/TiO$_2$ photocatalytic coatings for buildings, Build. Environ. 92 (2015) 734–742, https://doi.org/10.1016/j.buildenv.2015.05.028.

[25] P. Wolkoff, G.D. Nielsen, Organic compounds in indoor air—their relevance for perceived indoor air quality? Atmos. Environ. 35 (2001) 4407–4417, https://doi.org/10.1016/S1352-2310(01)00244-8.

[26] D. Won, R.L. Corsi, M. Rynes, Sorptive interactions between VOCs and indoor materials, Indoor Air 11 (2001) 246–256, https://doi.org/10.1034/j.1600-0668.2001.110406.x.

[27] D. Maskell, C.F. da Silva, K. Mower, R. Cheta, A. Dengel, R. Ball, M. Ansell, P. Walker, A. Shea, Properties of Bio-based Insulation Materials and Their Potential Impact on Indoor Air Quality, (2015) (Accessed 1 October 2018), https://researchportal.bath.ac.uk/en/publications/properties-of-bio-based-insulation-materials-and-their-potential.

[28] C.F. da Silva, D. Maskell, R. Ball, M. Ansell, The Physical, Chemical and Mechanical Properties of Eco-materials for Passive Indoor Environmental Control, (2014) (Accessed 1 October 2018), https://researchportal.bath.ac.uk/en/publications/the-physical-chemical-and-mechanical-properties-of-eco-materials-.

[29] C.F. da Silva, C. Rana, D. Maskell, A. Dengel, M.P. Ansell, R.J. Ball, Influence of eco-materials on indoor air quality, Int. J. Green Nanotechnol. Mater. Sci. Eng. 4 (2016), https://doi.org/10.1680/jgrma.16.00002.

[30] C.A. Redlich, J. Sparer, M.R. Cullen, Sick-building syndrome, Lancet 349 (1997) 1013–1016, https://doi.org/10.1016/S0140-6736(96)07220-0.

[31] P. Wargocki, D.P. Wyon, J. Sundell, G. Clausen, P.O. Fanger, The effects of outdoor

air supply rate in an office on perceived air quality, sick building syndrome (SBS) symptoms and productivity, Indoor Air 10 (2000) 222–236, https://doi.org/10.1034/j.1600-0668.2000.010004222.x.

[32] J.M. Daisey, A.T. Hodgson, Initial efficiencies of air cleaners for the removal of nitrogen dioxide and volatile organic compounds, Atmos. Environ. 23 (1967) 1885–1892, https://doi.org/10.1016/0004-6981(89)90514-3 1989.

[33] J.Y. Yoo, C.J. Park, K.Y. Kim, Y.-S. Son, C.-M. Kang, J.M. Wolfson, I.-H. Jung, S.-J. Lee, P. Koutrakis, Development of an activated carbon filter to remove NO_2 and HONO in indoor air, J. Hazard. Mater. 289 (2015) 184–189, https://doi.org/10.1016/j.jhazmat.2015.02.038.

[34] C.L. Bianchi, C. Pirola, E. Selli, S. Biella, Photocatalytic NOx abatement: the role of the material supporting the TiO_2 active layer, J. Hazard. Mater. 211–212 (2012) 203–207, https://doi.org/10.1016/j.jhazmat.2011.10.095.

[35] Air Quality Guide for Nitrogen Dioxide, EPA-456/F-11-003 https://cfpub.epa.gov/airnow/index.cfm?action=pubs.aqiguidenox.

[36] Y. Shimizu, D. Koba, H. Saitoh, S. Takase, A NO_x sensor using solid electrolyte impedance transducer and perovskite-type oxide receptor, ECS Trans. 1 (2006) 131–140, https://doi.org/10.1149/1.2215549.

[37] V.V. Plashnitsa, T. Ueda, P. Elumalai, N. Miura, NO_2 sensing performances of planar sensor using stabilized zirconia and thin-NiO sensing electrode, Sens. Actuators B Chem. 130 (2008) 231–239, https://doi.org/10.1016/j.snb.2007.07.127.

[38] N. Masson, R. Piedrahita, M. Hannigan, Approach for quantification of metal oxide type semiconductor gas sensors used for ambient air quality monitoring, Sens. Actuators B Chem. 208 (2015) 339–345, https://doi.org/10.1016/j.snb.2014.11.032.

[39] R. Baron, J. Saffell, Amperometric gas sensors as a low cost emerging technology platform for air quality monitoring applications: a review, ACS Sens. 2 (2017) 1553–1566, https://doi.org/10.1021/acssensors.7b00620.

[40] Y. Gönüllü, G.C.M. Rodríguez, B. Saruhan, M. Ürgen, Improvement of gas sensing performance of TiO_2 towards NO_2 by nano-tubular structuring, Sens. Actuators B Chem. 169 (2012) 151–160, https://doi.org/10.1016/j.snb.2012.04.050.

[41] T. Xie, N. Sullivan, K. Steffens, B. Wen, G. Liu, R. Debnath, A. Davydov, R. Gomez, A. Motayed, UV-assisted room-temperature chemiresistive NO_2 sensor based on TiO_2 thin film, J. Alloys. Compd. 653 (2015) 255–259, https://doi.org/10.1016/j.jallcom.2015.09.021.

[42] I. Karaduman, D.E. Yıldız, M.M. Sincar, S. Acar, UV light activated gas sensor for NO_2 detection, Mater. Sci. Semicond. Process. 28 (2014) 43–47, https://doi.org/10.1016/j.mssp.2014.04.011.

[43] D.M. Tobaldi, R.C. Pullar, M.P. Seabra, J.A. Labrincha, Fully quantitative X-ray characterisation of evonik aeroxide TiO_2 P25°, Mater. Lett. 122 (2014) 345–347, https://doi.org/10.1016/j.matlet.2014.02.055.

[44] B. Ohtani, O.O. Prieto-Mahaney, D. Li, R. Abe, What is Degussa (Evonik) P25? Crystalline composition analysis, reconstruction from isolated pure particles and photocatalytic activity test, J. Photochem. Photobiol. Chem. 216 (2010) 179–182, https://doi.org/10.1016/j.jphotochem.2010.07.024.

[45] A. Giampiccolo, R. Ball, M. Ansell, D. Maskell, Synthesis of Co-doped TiO_2 Nanostructures for Novel Photo-catalytic Coatings, (2014) (Accessed 1 October 2018), https://researchportal.bath.ac.uk/en/publications/synthesis-of-co-doped-tio2-nanostructures-for-novel-photo-catalyt.

[46] B. O'Regan, M. Grätzel, A low-cost, high-efficiency solar cell based on dye-sensitized colloidal TiO_2 films, Nature 353 (1991) 737–740, https://doi.org/10.1038/353737a0.

[47] T. Luttrell, S. Halpegamage, J. Tao, A. Kramer, E. Sutter, M. Batzill, Why is anatase a better photocatalyst than rutile? – Model studies on epitaxial TiO_2 films, Sci. Rep. 4 (2014) 4043, https://doi.org/10.1038/srep04043.

[48] G. Odling, N. Robertson, Why is anatase a better photocatalyst than rutile? The importance of free hydroxyl radicals, ChemSusChem 8 (2015) 1838–1840, https://doi.org/10.1002/cssc.201500298.

[49] A.C. Larson, R.B. Von Dreele, General Structure Analysis System (GSAS), Los Alamos National Laboratory Report LAUR, 2004.

[50] B.H. Toby, EXPGUI, a graphical user interface for GSAS, J. Appl. Crystallogr. 34 (2001) 210–213, https://doi.org/10.1107/S0021889801002242.

[51] G. Caglioti, A. Paoletti, F.P. Ricci, On resolution and luminosity of a neutron diffraction spectrometer for single crystal analysis, Nucl. Instrum. Methods. 9 (1960) 195–198, https://doi.org/10.1016/0029-554X(60)90101-4.

[52] P. Scardi, M. Ortolani, M. Leoni, WPPM: microstructural analysis beyond the rietveld method, Mater. Sci. Forum. 651 (2010) 155–171, https://doi.org/10.4028/www.scientific.net/MSF.651.155.

[53] M. Leoni, T. Confente, P. Scardi, PM2K: a flexible program implementing Whole Powder Pattern Modelling, Z. Für Krist. (Suppl. 23) (2006) 249–254, https://doi.org/10.1524/zksu.2006.suppl_23.249.

[54] P. Scardi, M. Leoni, Whole Powder Pattern Modelling: Theory and Applications, in: Diffraction Analysis of the Microstructure of Materials, Springer-Verlag, Eric J. Mittemeijer, Paolo Scardi, Berlin, 2004, pp. 51–92.

[55] A. Dolgonos, T.O. Mason, K.R. Poeppelmeier, Direct optical band gap measurement in polycrystalline semiconductors: a critical look at the Tauc method, J. Solid State Chem. 240 (2016) 43–48, https://doi.org/10.1016/j.jssc.2016.05.010.

[56] S.S. Lucas, V.M. Ferreira, J.L.B. de Aguiar, Incorporation of titanium dioxide nanoparticles in mortars — influence of microstructure in the hardened state properties and photocatalytic activity, Cem. Concr. Res. 43 (2013) 112–120, https://doi.org/10.1016/j.cemconres.2012.09.007.

[57] U.I. Gaya, A.H. Abdullah, Heterogeneous photocatalytic degradation of organic contaminants over titanium dioxide: a review of fundamentals, progress and problems, J. Photochem. Photobiol. C Photochem. Rev. 9 (2008) 1–12, https://doi.org/10.1016/j.jphotochemrev.2007.12.003.

[58] F.L. Toma, G. Bertrand, D. Klein, C. Coddet, Photocatalytic removal of nitrogen oxides via titanium dioxide, Environ. Chem. Lett. 2 (2004) 117–121, https://doi.org/10.1007/s10311-004-0087-2.

[59] T. Wagner, C.-D. Kohl, C. Malagù, N. Donato, M. Latino, G. Neri, M. Tiemann, UV light-enhanced NO2 sensing by mesoporous In_2O_3: interpretation of results by a new sensing model, Sens. Actuators B Chem. 187 (2013) 488–494, https://doi.org/10.1016/j.snb.2013.02.025.

[60] S. Trocino, P. Frontera, A. Donato, C. Busacca, L.A. Scarpino, P. Antonucci, G. Neri, Gas sensing properties under UV radiation of In_2O_3 nanostructures processed by electrospinning, Mater. Chem. Phys. 147 (2014) 35–41, https://doi.org/10.1016/j.matchemphys.2014.03.057.

[61] H. Zhang, J.F. Banfield, Thermodynamic analysis of phase stability of nanocrystalline titania, J. Mater. Chem. 8 (1998) 2073–2076, https://doi.org/10.1039/a802619j.

[62] H. Zhang, M. Finnegan, J.F. Banfield, Preparing single-phase nanocrystalline anatase from amorphous titania with particle sizes tailored by temperature, Nano Lett. 1 (2001) 81–85, https://doi.org/10.1021/nl0055198.

[63] S.L. Isley, R.L. Penn, Relative brookite and anatase content in sol − Gel-Synthesized titanium dioxide nanoparticles, J. Phys. Chem. B 110 (2006) 15134–15139, https://doi.org/10.1021/jp061417f.

[64] D.M. Tobaldi, R.C. Pullar, R. Binions, A. Belen Jorge, P.F. McMillan, M. Saeli, M.P. Seabra, J.A. Labrincha, Influence of sol counter-ions on the visible light induced photocatalytic behaviour of TiO_2 nanoparticles, Catal. Sci. Technol. 4 (2014) 2134, https://doi.org/10.1039/c4cy00423j.

[65] A.C. Ferrari, J.C. Meyer, V. Scardaci, C. Casiraghi, M. Lazzeri, F. Mauri, S. Piscanec, D. Jiang, K.S. Novoselov, S. Roth, A.K. Geim, Raman Spectrum of graphene and graphene layers, Phys. Rev. Lett. 97 (2006) 187401, , https://doi.org/10.1103/PhysRevLett.97.187401.

[66] A.K. Gupta, T.J. Russin, H.R. Gutiérrez, P.C. Eklund, Probing graphene edges via raman scattering, ACS Nano 3 (2009) 45–52, https://doi.org/10.1021/nn8003636.

[67] F. Sordello, G. Zeb, K. Hu, P. Calza, C. Minero, T. Szkopek, M. Cerruti, Tuning TiO_2 nanoparticle morphology in graphene–TiO_2 hybrids by graphene surface modification, Nanoscale 6 (2014) 6710–6719, https://doi.org/10.1039/C4NR01322K.

[68] A.S. Marfunin, Physics of Minerals and Inorganic Materials: An Introduction, Springer-Verlag, Berlin Heidelberg, 1979, www.springer.com/gp/book/9783642670466 (Accessed October 1, 2018).

[69] M. Koelsch, S. Cassaignon, J. Guillemoles, J. Jolivet, Comparison of optical and electrochemical properties of anatase and brookite TiO_2 synthesized by the sol–gel method, Thin Solid Films 403–404 (2002) 312–319, https://doi.org/10.1016/S0040-6090(01)01509-7.

[70] D.M. Tobaldi, R.C. Pullar, L. Durães, T. Matias, M.P. Seabra, J.A. Labrincha, Truncated tetragonal bipyramidal anatase nanocrystals formed without use of capping agents from the supercritical drying of a TiO_2 sol, CrystEngComm 18 (2016) 164–176, https://doi.org/10.1039/C5CE02112J.

[71] N. Serpone, D. Lawless, R. Khairutdinov, Size effects on the photophysical properties of colloidal anatase TiO_2 particles: size quantization versus direct transitions in this indirect semiconductor? J. Phys. Chem. 99 (1995) 16646–16654, https://doi.org/10.1021/j100045a026.

[72] T. Xie, A. Rani, B. Wen, A. Castillo, B. Thomson, R. Debnath, T.E. Murphy, R.D. Gomez, A. Motayed, The effects of surface conditions of TiO_2 thin film on the UV assisted sensing response at room temperature, Thin Solid Films 620 (2016) 76–81, https://doi.org/10.1016/j.tsf.2016.07.075.

[73] J. Esmaeilzadeh, E. Marzbanrad, C. Zamani, B. Raissi, Fabrication of undoped-TiO_2 nanostructure-based NO_2 high temperature gas sensor using low frequency AC electrophoretic deposition method, Sens. Actuators B Chem. 161 (2012) 401–405, https://doi.org/10.1016/j.snb.2011.10.051.

[74] M.G. Manera, A. Taurino, M. Catalano, R. Rella, A.P. Caricato, R. Buonsanti, P.D. Cozzoli, M. Martino, Enhancement of the optically activated NO_2 gas sensing response of brookite TiO_2 nanorods/nanoparticles thin films deposited by matrix-assisted pulsed-laser evaporation, Sens. Actuators B Chem. 161 (2012) 869–879, https://doi.org/10.1016/j.snb.2011.11.051.

[75] B. Saruhan, A. Yüce, Y. Gönüllü, K. Kelm, Effect of Al doping on NO_2 gas sensing of TiO_2 at elevated temperatures, Sens. Actuators B Chem. 187 (2013) 586–597, https://doi.org/10.1016/j.snb.2013.04.111.

[76] R. Vyas, S. Sharma, P. Gupta, Y.K. Vijay, A.K. Prasad, A.K. Tyagi, K. Sachdev, S.K. Sharma, Enhanced NO_2 sensing using ZnO–TiO_2 nanocomposite thin films, J. Alloys. Compd. 554 (2013) 59–63, https://doi.org/10.1016/j.jallcom.2012.11.059.

[77] Y. Gönüllü, A.A. Haidry, B. Saruhan, Nanotubular Cr-doped TiO_2 for use as high-temperature NO_2 gas sensor, Sens. Actuators B Chem. 217 (2015) 78–87, https://doi.org/10.1016/j.snb.2014.11.065.

[78] Z. Zhu, S.-J. Lin, C.-H. Wu, R.-J. Wu, Synthesis of TiO_2 nanowires for rapid NO_2 detection, Sens. Actuators Phys. 272 (2018) 288–294, https://doi.org/10.1016/j.sna.2018.02.006.

[79] B.J. Hansen, N. Kouklin, G. Lu, I.-K. Lin, J. Chen, X. Zhang, Transport, analyte detection, and opto-electronic response of p-Type CuO nanowires, J. Phys. Chem. C 114 (2010) 2440–2447, https://doi.org/10.1021/jp908850j.

[80] R. Kumar, N. Goel, M. Kumar, UV-activated MoS2 based fast and reversible NO2 sensor at room temperature, ACS Sens. 2 (2017) 1744–1752, https://doi.org/10.1021/acssensors.7b00731.

[81] W. Han, Z. Li, Y. Li, X. Fan, F. Zhang, G. Zhang, W. Peng, The promoting role of different carbon allotropes cocatalysts for semiconductors in photocatalytic energy generation and pollutants degradation, Front. Chem. 5 (2017), https://doi.org/10.3389/fchem.2017.00084.

[82] R. Sellappan, J. Sun, A. Galeckas, N. Lindvall, A. Yurgens, A.Y. Kuznetsov, D. Chakarov, Influence of graphene synthesizing techniques on the photocatalytic performance of graphene–TiO_2 nanocomposites, Phys. Chem. Chem. Phys. 15 (2013) 15528–15537, https://doi.org/10.1039/C3CP52457D.

[83] Y.T. Liang, B.K. Vijayan, K.A. Gray, M.C. Hersam, Minimizing graphene defects enhances titania nanocomposite-based photocatalytic reduction of CO_2 for improved solar fuel production, Nano Lett. 11 (2011) 2865–2870, https://doi.org/10.1021/nl2012906.

[84] A. Trapalis, N. Todorova, T. Giannakopoulou, N. Boukos, T. Speliotis, D. Dimotikali, J. Yu, TiO2/graphene composite photocatalysts for NO_x removal: a comparison of surfactant-stabilized graphene and reduced graphene oxide, Appl. Catal. B Environ. 180 (2016) 637–647, https://doi.org/10.1016/j.apcatb.2015.07.009.

[85] H. Zhang, X. Lv, Y. Li, Y. Wang, J. Li, P25-graphene composite as a high performance photocatalyst, ACS Nano 4 (2010) 380–386, https://doi.org/10.1021/nn901221k.

[86] R. Zouzelka, J. Rathousky, Photocatalytic abatement of NO_x pollutants in the air using commercial functional coating with porous morphology, Appl. Catal. B Environ. 217 (2017) 466–476, https://doi.org/10.1016/j.apcatb.2017.06.009.

[87] F. Dong, Z. Zhao, Y. Sun, Y. Zhang, S. Yan, Z. Wu, An advanced semimetal–organic Bi spheres–g-C_3N_4 nanohybrid with SPR-Enhanced visible-light photocatalytic performance for NO purification, Environ. Sci. Technol. 49 (2015) 12432–12440, https://doi.org/10.1021/acs.est.5b03758.

[88] Y. Ohko, Y. Nakamura, A. Fukuda, S. Matsuzawa, K. Takeuchi, Photocatalytic oxidation of nitrogen dioxide with TiO_2 thin films under continuous UV-light illumination, J. Phys. Chem. C 112 (2008) 10502–10508, https://doi.org/10.1021/jp802959c.